J. Fluid Mech. (2005), *vol.* 538, *pp.* 269–289.
doi:10.1017/S0022112005005367 Printed in the United Kingdom

Effects of an opening on pressure wave propagation in a tube

By B. AUVITY[1] AND M. BELLENOUE[2]

[1]Laboratoire de Thermocinétique (CNRS UMR 6607), Ecole Polytechnique de l'Université de Nantes, Nantes, France

[2]Laboratoire de Combustion et de Détonique (CNRS UPR 9028), E.N.S.M.A., Poitiers, France

(Received 8 April 2004 and in revised form 8 March 2005)

This paper focuses on the effects of an opening placed along a tube on the propagation of a pressure wavefront. Such a configuration has been chosen for its relevance to many of the countermeasures envisaged in reducing strong pressure transients in tunnels due to the entry of high-speed trains (this installation includes a perforated entrance hood and ventilation shaft). We will start by establishing that when a compression wavefront passes through an opening, the front is split into an infinite number of smaller pressure steps, with their amplitude expressed as the terms of a mathematical series. The main parameter of the series is a transmission coefficient of the opening. The shape of each of the smaller pressure steps is driven by the transmission–reflection process that takes place at the opening. Both experimental and numerical studies have been carried out to carefully estimate both the transmission coefficient and the shape of the transmitted and reflected pressure waves. Three major parameters are identified: the relative surface area of the opening to the tube cross-section, the ratio of the incident front length to the longitudinal opening length, and the incident front amplitude.

It will be shown that the transmission coefficient decreases exponentially with the relative surface area of the opening and is significantly influenced by the incident front amplitude. Both the length and shape of the transmitted front are similar to those of the incident front. The reflected front length, however, increases linearly with the incident front length as well as with the longitudinal opening length. The shape of the reflected front is greatly influenced by the incident front length. A linear analysis has been conducted and shows that the transmission coefficient can be predicted in a straightforward manner. These results are deemed to be of help not only in the design of countermeasures for the train/tunnel entry problem, but also for technological applications involving transient pressure pulses in branched pipe flows (e.g. pulsed flow in exhaust pipes).

1. Introduction

With the development of high-speed train networks, pressure waves in tunnels have raised a number of problems, including ear discomfort for train passengers and sonic booms generated at tunnel exits. These phenomena are closely correlated with strong pressure gradients in the tunnel. Many solutions have been envisaged and tested in order to reduce the pressure gradient in tunnels. The aim of these solutions is to increase the pressure rise time in the tunnel and/or to allow for a partial discharge of compressed air into the surrounding atmosphere or into an adjacent tube. The

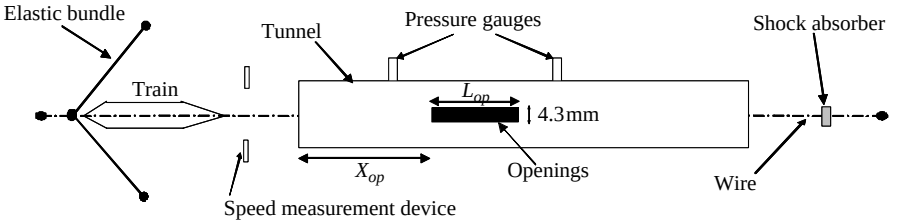

FIGURE 1. Schematic diagram of the experimental apparatus.

most common solutions consist of lengthening the train nose (Maeda *et al.* 1993; Iida *et al.* 1996), adding a constant cross-section hood ahead of the main tunnel section (Bellenoue Auvity & Kageyama 2001), adding a flared hood (Howe 1999) or a perforated hood (Ozawa & Maeda 1988; Bellenoue & Kageyama 2002; Howe *et al.* 2003), and making use of side branches (Henson & Pope 1997). These last two countermeasures involve the propagation of pressure waves within a perforated tunnel.

In the case of a perforated hood, air directly discharges into the surrounding atmosphere. An expansion wave is instantaneously formed in the hood, while the primary compression wave has not yet been completely generated. Recent work undertaken by Howe *et al.* (2003) yielded a description of the phenomena encountered for this case; they gave an analytical prediction, which was satisfactorily validated by experiments at the model scale. Their research however was restricted to openings located close to the tunnel entrance. In the case of side branches, which tend to be located far from the tunnel entrance, a travelling wave is generated in the branched pipe and then returns to the main tunnel as an expansion wave with a time lag that depends on the pipe length. This expansion wave perturbs the transmission–reflection process taking place at the junction; however, a clear and complete description of the transmission–reflection process occurring as a pressure wave passes an opening still needs to be provided.

In this paper, the generic configuration of a fully formed pressure wave propagating within a thin perforated tube will be examined. A complete description of the effects of an opening on the compression wavefront, without being limited to the case where the opening is close to the tube entrance, is proposed. The main parameters will be clearly exposed and their individual effect closely assessed using both experimental and numerical approaches. Lastly, a simple analytical development will be put forward that enables a prediction of the pressure wave generated by entry of a slender body into a tube in the presence of an opening.

2. Presentation of experimental apparatus and measurement techniques

2.1. *Presentation of the compression wavefront generator*

Compression wavefronts are produced by the entry of a slender body into a tube. The experimental apparatus available at the L.C.D. facility (Bellenoue *et al.* 2001; Auvity, Bellenoue & Kageyama 2001) has been used for this study. A diagram of the set-up is displayed in figure 1.

The slender body is a circular cylinder 600 mm in length and 25 mm in diameter. The body nose and tail geometries are fixed: the body nose $L_{nose} = 40$ mm long with an elliptical shape and the tail is flat. The tube length and diameter are $L_{tube} = 4.4$ m and $D_{tube} = 44$ mm (area $S_{tube} = 1520.5\,\text{mm}^2$), respectively. The tube and moving body

lengths are chosen so as to prevent the interaction of observed phenomena with both the expansion wave resulting from compression wave reflection at the tunnel exit and the expansion wave created by body tail entry into the tube.

The slender body is launched by means of an elastic-bundle catapult and then guided onto a 0.8 mm diameter wire monorail. With this system a body can reach a speed of $50\,\mathrm{m\,s^{-1}}$ (i.e. a Mach number equal to 0.15). The moving body speed is measured for each run with a level of uncertainty of less than 2 % (Bellenoue *et al.* 2001).

The moving body/tube blockage ratio (body section area divided by tube section area) is 0.32. This value has been chosen for the present study so that the maximum compression wave amplitude reached for the maximum moving body speed is: $\Delta p_{max} \approx 1600\,\mathrm{Pa}$. This value lies close to the maximum encountered on high-speed train networks.

The tube diameter determines the magnitude of frictional effects during pressure wavefront propagation. A competition is actually observed between nonlinear steepening effects that occur naturally when a one-dimensional compression wavefront propagates within a semi-infinite domain and smoothing effects due to friction on the tube wall. Under the conditions discussed, no noticeable smoothing or steepening effects have been observed for propagation distances on the order of 40 tube diameters.

A non-dimensional pressure C_p is used herein, as defined by

$$C_p = \frac{p - p_0}{\frac{1}{2}\rho_0 V_{body}^2} \tag{1}$$

where p_0 and ρ_0 are respectively the pressure and density under atmospheric conditions and V_{body} is the body speed.

A non-dimensional time scale t_a may also be defined, as follows:

$$t_a = \frac{V_{body} t}{L_{ref}}. \tag{2}$$

where L_{ref} is a reference length set equal to the body nose length (i.e. $L_{ref} = L_{nose} = 40\,\mathrm{mm}$). t_a equals zero when the tip of the body nose is entering the tube.

A non-dimensional pressure gradient can then be defined as

$$K_{gr} = \frac{\mathrm{d}Cp}{\mathrm{d}t_a}. \tag{3}$$

Figure 2 presents typical compression waves generated for various body speeds using the non-dimensional coordinate system (C_p, t_{ashift}). t_{ashift} is equivalent to the non-dimensional time introduced above, except that an additional shift has been included. This shift corresponds to the time taken by the compression wave to propagate from the tube entrance to the microphone position, $X_{\mu phone\,1}$:

$$t_{ashift} = t_a - \frac{V_{body} X_{\mu phone\,1}}{c_0 L_{ref}} = \frac{V_{body}}{L_{ref}}\left(t - \frac{X_{\mu phone\,1}}{c_0}\right). \tag{4}$$

Using t_{ashift}, all compression wavefronts reach $\mathrm{X}_{\mu phone\,1}$ at the same non-dimensional time. In the coordinate system shown in figure 2, the compression wavefronts are similar as regards body speed. The maximum value of C_p, C_{pmax}, obtained at the end of the front is almost unchanged over the investigated range of body speeds: 20–$50\,\mathrm{m\,s^{-1}}$. This value is in agreement with the semi-empirical formulation derived by Ozawa (1979).

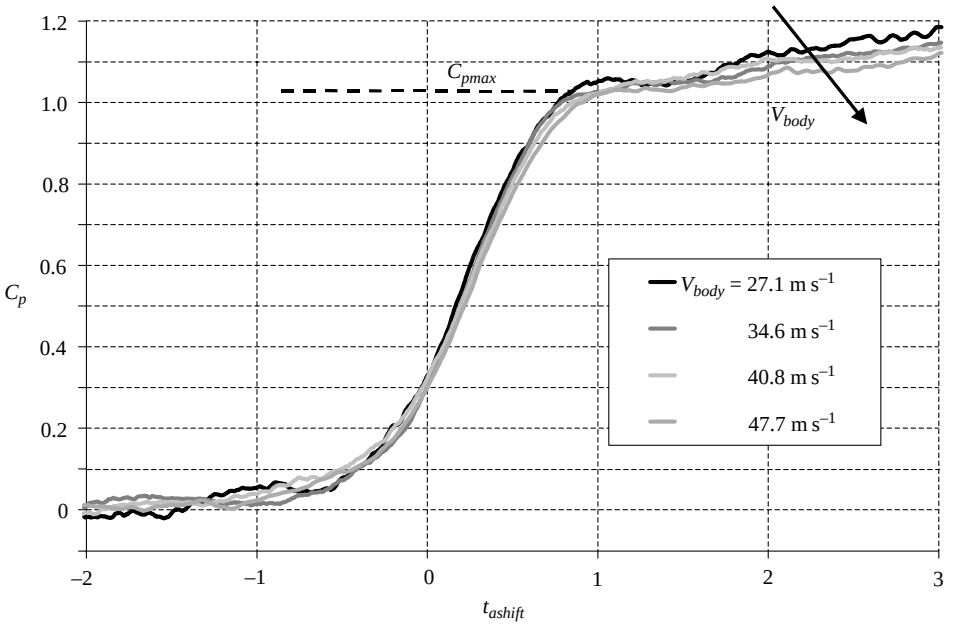

FIGURE 2. Compression waves generated by the apparatus in a non-dimensional coordinate system (C_p, t_{ashift}).

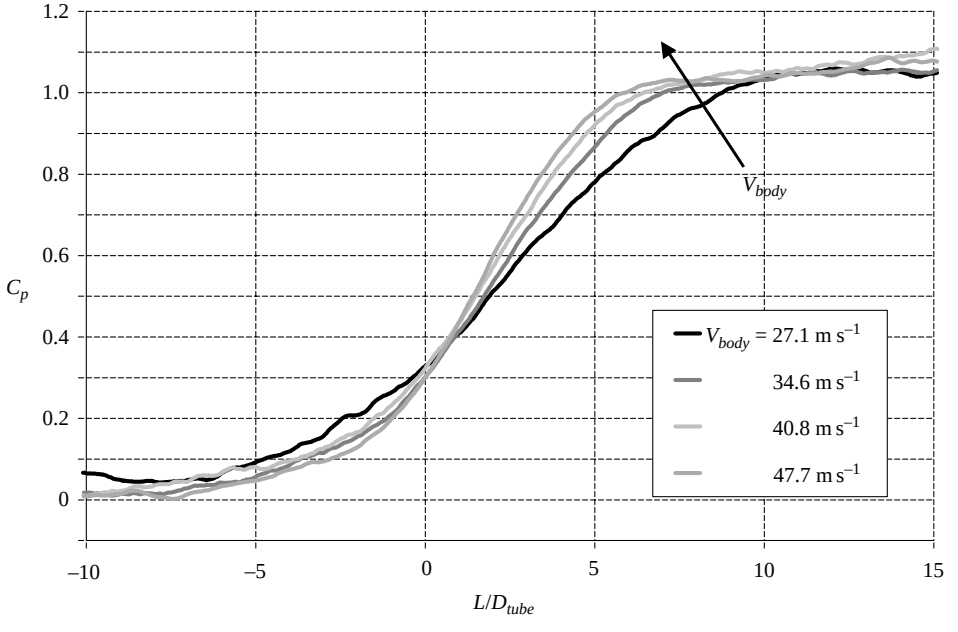

FIGURE 3. Compression waves generated by the apparatus within a spatial representation.

Figure 3 exhibits a spatial representation of the compression waves presented in figure 2, as based on the time history measured at the transducer point. The x-axis coordinate is a non-dimensional length, L/D_{tube}, deduced from the physical time

according to the following simple relation:

$$\frac{L}{D_{tube}} = \frac{c_0}{V_{body}} \frac{L_{ref}}{D_{tube}} t_{ashift} = \frac{c_0}{D_{tube}} \left(t - \frac{X_{\mu phone\ 1}}{c_0} \right). \tag{5}$$

For faster moving bodies, the compression wavefront shortens in length. Given that the non-dimensional duration of the fronts remains unchanged, the spatial extent of the compression front is inversely proportional to the speed of the moving body.

In summary, the maximum amplitude of the compression wavefront increases with the square of moving body speed, whereas the spatial length increases linearly. The major drawback of this experimental set-up is that compression waves with different amplitudes yet equal front lengths cannot be produced without changing the body nose length and/or tube entrance geometry.

2.2. *Pressure measurements*

Compression waves have been measured using Bruel & Kjaer 1/4-in. piezoelectric microphones (type 4136) in association with a conditioner amplifier (Nexus type 2690 0S4). The measurement range of the transducer is 1 p.s.i. (6900 Pa). For the maximum pressure amplitude (1600 Pa), the cumulative relative precision error for pressure measurements is less than 1 %. The sensitive surface of the microphone is mounted flush with the inner tube surface. The frequency response of the pressure transducer is 90 kHz at −2 dB. In order to capture transient phenomena with a typical time of 100 μs, pressure signals have been sampled by means of a 12-bit oscilloscope at a frequency of 200 kHz. No filter has been used in this procedure.

Pressure measurements are performed both upstream and downstream of the opening (see figure 1). The distance between tube entrance and the first microphone ($X_{\mu phone\ 1}$), the distance between $X_{\mu phone\ 1}$ and the beginning of the opening (X_{op}) and the distance between the end of the opening ($X_{op} + L_{op}$) and the second microphone ($X_{\mu phone\ 2}$) have all been set at greater than $10D_{tube}$ so as to ensure the one-dimensionality of the measured pressure waves originating from the tube entrance and/or the opening: $X_{\mu phone\ 1} = 13D_{tube}$, $X_{op} = 25D_{tube}$ and $X_{\mu phone\ 2} = 39D_{tube}$. Bellenoue, Moriniere & Kageyama (2002) proved that a distance of 4 tube diameters was indeed sufficient to ensure the one-dimensionality of pressure wavefronts.

2.3. *Opening geometry*

A generic geometric configuration has been chosen for the opening, consisting of a slit 4.3 mm wide. Two types of slits with a length of either $L_{op} = 0.5D_{tube}$ or $L_{op} = 0.2D_{tube}$ have been used. A modification in the opening surface area is introduced by varying the number of slits (from 1 to 4 at the same location) and/or by changing the type of slit. When there is more than one slit, they are distributed equally around the tube perimeter. Table 1 presents all configurations tested within the scope of these experiments. The relative opening surface area, as a percentage of tube cross-section, varies from 2.5 % to 26.4 %.

The tube thickness is 3 mm. The time required to travel twice this distance at the speed of sound is approximately 18 μs; this time lag is not noticeable under experimental conditions and the opening is then considered as being directly correlated with atmospheric conditions. The opening length, L_{op}, is chosen to be small in comparison with tube diameter. In the experiments, the compression wavefront length is on the order of 10 tube diameters (see figure 3), and the opening length is no more than half the tube diameter. The experimental study is limited to the case where the pressure front length, L_{front}, is much greater than the opening length, L_{op}. It proved

Test case	Number of openings	L_{op}	S_{op}/S_{tube}
1	1	$0.2D_{tube}$	2.5 %
2	2	$0.2D_{tube}$	5.0 %
3	3	$0.2D_{tube}$	7.5 %
4	4	$0.2D_{tube}$	10.0 %
5	1	$0.5D_{tube}$	6.2 %
6	2	$0.5D_{tube}$	12.4 %
7	3	$0.5D_{tube}$	18.7 %
8	4	$0.5D_{tube}$	26.4 %

TABLE 1. Geometric opening configurations tested in the experiments.

impossible with the experimental apparatus to explore the range where L_{op} was of the same order as L_{front}. A very short compression wavefront of about one tube diameter in length cannot be generated, even with the entry of a flat-nosed body into the tube. The length of the compression wavefront generated with a flat-nosed body for a body/tube blockage ratio of 0.32 and $V_{body} = 45.0\,\mathrm{m\,s^{-1}}$ is in fact on the order of seven tube diameters (Auvity 1998).

3. Presentation of the basic phenomena

This section introduces the major relevant parameters and has been based on experimental observations. Figure 4 presents an (x, t) diagram along with pressure signals recorded at positions $X_{\mu phone\,1}$ and $X_{\mu phone\,2}$. This experiment has been conducted under the conditions of Test case 6 and $V_{body} = 42.0\,\mathrm{m\,s^{-1}}$. The OC1h and OC1e lines represent respectively the head and tail of compression wavefront OC1 generated by the body nose entry into the tube. As compression front OC1 passes through the opening, air discharge occurs, thereby creating an expansion wavefront propagating back into the tube. This expansion wave, called OD1, may be seen on the pressure signal at $X_{\mu phone\,1}$ as the second (negative) pressure front. The air discharge occurring as the compression wavefront propagates through the opening is such that compression wavefront OC1, recorded at position $X_{\mu phone\,2}$, displays an amplitude C_{p1} smaller than C_{p0}.

Upon reaching the tube entrance, wavefront OD1 reflects back into the tube and changes sign to become a compression wavefront, OC2. Front OC2 may be detected at time 30 ms and at position $X_{\mu phone\,1}$; this wavefront at position $X_{\mu phone\,2}$ corresponds to the second step in the pressure signal. Like wavefront OC1, the amplitude of wavefront OC2, C_{p2}, is reduced after passing through the opening. An expansion wavefront OD3 is then produced as wavefront OC2 passes through the opening. Wavefront OD2 reflects back at the tube entrance just like wavefront OC3 and is detected as the third step in the pressure signal at position $X_{\mu phone\,2}$, with an amplitude of C_{p3}.

Following the three positive pressure steps on the pressure signal at position $X_{\mu phone\,2}$, a pressure drop occurs that corresponds to both the passing of the expansion wavefront due to the reflection of wavefront OC1 at the tube exit and the passing of the expansion front generated by the moving body tail entry.

The effect of an opening placed along a tube on a compression wavefront is thus clearly illustrated based on the present set of experiments. In the absence of an opening, the initial compression wavefront generated by the body nose entry (first step in the pressure signal at position $X_{\mu phone\,1}$) propagates inside the tube and reflects

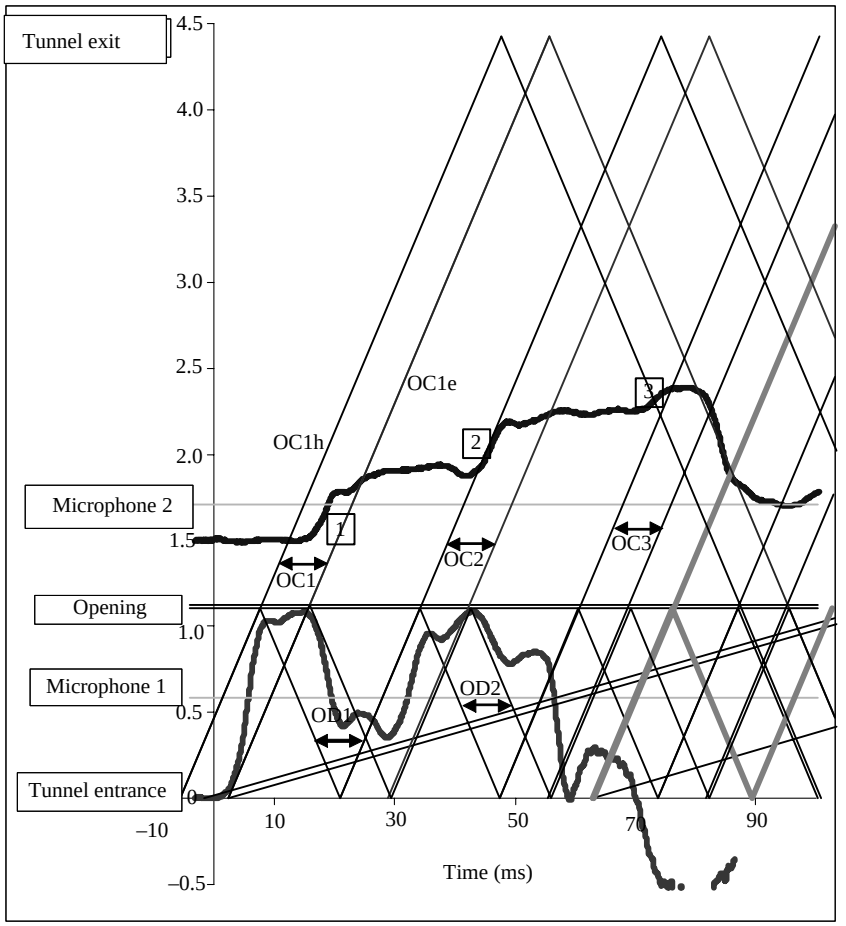

FIGURE 4. (x, t) diagram and pressure signal at positions $X_{\mu phone\ 1}$ and $X_{\mu phone\ 2}$ along the tunnel.

several times at both the tube entrance and exit. Eventually, the front steepens during propagation. Introducing an opening significantly modifies the transient pressure in the tube and, in particular, evens out the pressure rise downstream of the opening, i.e. increases the length of the compression wavefront. Under the conditions tested herein, three reduced-compression fronts were clearly observed.

Based on the above description, the effect of an opening on a pressure wavefront with an amplitude of C_{pi}, called the *incident front*, may be summarized as follows: an opening generates an expansion wave that propagates both downstream and upstream of the opening. Downstream of the opening, this expansion wave is superimposed upon the initial compression wave, such that the resultant *transmitted wavefront* C_{pt} has a reduced amplitude compared to the incident front C_{pi}. The reflected wave is composed solely of the expansion wave created at the opening. The amplitude of the reflected front will be denoted C_{pr}.

We will now define a *transmission coefficient* α for each opening as the ratio of the transmitted front amplitude to the incident front amplitude, i.e.

$$\alpha = \frac{C_{pt}}{C_{pi}} = \frac{\Delta p_t}{\Delta p_i}. \tag{6}$$

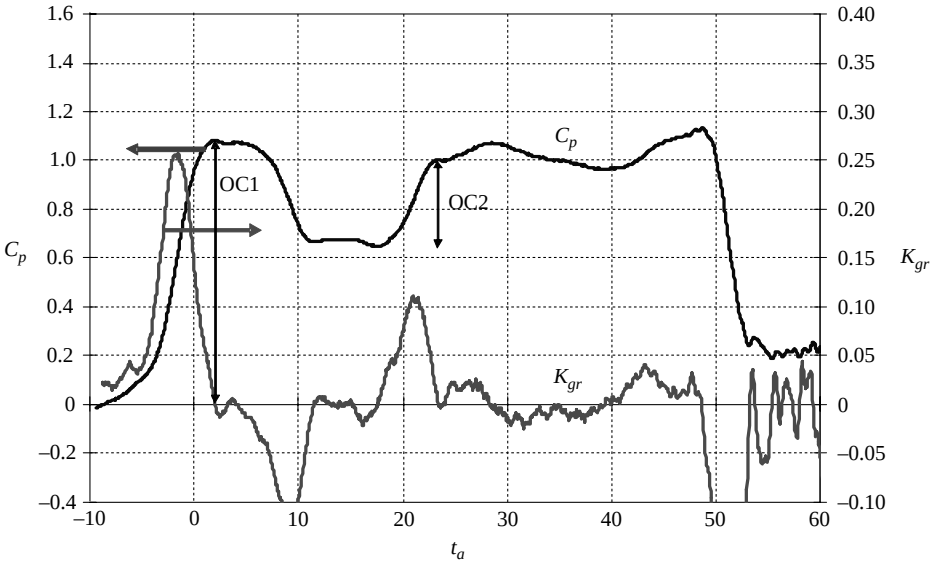

FIGURE 5. Pressure signal and associated pressure gradient at position $X_{\mu phone\,1}$ for Test case 4 and $V_{body} = 40.0\,\mathrm{m\,s^{-1}}$.

By comparing the absolute non-dimensional amplitude of these various wavefronts, the following may be written:

$$C_{pi} = C_{pt} + C_{pr} \quad \text{or} \quad \Delta p_i = \Delta p_t + \Delta p_r. \tag{7}$$

This then yields

$$\frac{\Delta p_r}{\Delta p_i} = \frac{C_{pr}}{C_{pi}} = 1 - \alpha. \tag{8}$$

Figure 5 (respectively figure 6) presents the pressure signal and associated pressure gradient measured at position $X_{\mu phone\,1}$ (respectively $X_{\mu phone\,2}$), as obtained from Test case 4 (see § 2.3 for further details).

The definition of α then leads to the following expression:

$$C_{pt1} = C_{p1} = \alpha\, C_{p0} \quad \text{and} \quad C_{pr1} = (1-\alpha)\, C_{po}.$$

Consequently,

$$C_{pt2} = C_{p2} = \alpha\, C_{pr1} = \alpha\,(1-\alpha)\, C_{p0} \quad \text{and} \quad C_{pr2} = (1-\alpha)\, C_{pr1} = (1-\alpha)^2\, C_{p0}.$$

Hence:

$$C_{pt3} = C_{p3} = \alpha\, C_{pr2} = \alpha\,(1-\alpha)^2\, C_{p0}.$$

In summary, if no pressure wave interferes with the process, the effect of an opening on a pressure wavefront of amplitude C_{p0} is to split the front into an infinite number of smaller pressure steps, each with an amplitude of C_{pi}, $i \geqslant 1$ for which

$$\sum_{i \geqslant 1} C_{pi} = C_{p0} \tag{9}$$

and

$$C_{pi} = \alpha(1-\alpha)^{(i-1)} C_{p0} \quad \text{for} \quad i \geqslant 1. \tag{10}$$

Test number	C_{p0}	C_{p1}	C_{p2} (exp)	C_{p2} (Eq. (10))	C_{p3} (exp.)	C_{p3} (Eq. (10))	$\left(\sum_{i=1}^{3} C_{pi}\right)_{exp}$	$\left(\sum_{i=1}^{3} C_{pi}\right)_{Eq.\,(10)}$
4	1.08	0.54	0.25	0.27	0.10	0.13	0.90	0.94
6	1.08	0.46	0.27	0.26	0.11	0.15	0.84	0.87
7	1.05	0.28	0.24	0.20	0.14	0.15	0.66	0.63

TABLE 2. Experimental validation of equations (9) and (10).

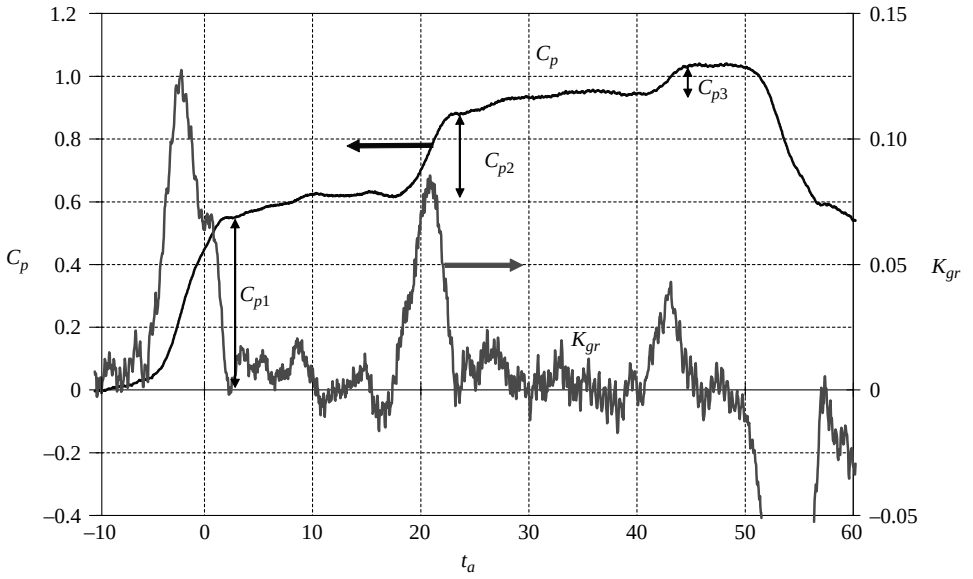

FIGURE 6. Pressure signal and associated pressure gradient at position $X_{\mu phone\ 2}$ for Test case 4 and $V_{body} = 40.0\,\mathrm{m\,s^{-1}}$.

With the present experiments, as mentioned above, a pressure drop due to tail train entry occurs after the third step, such that pressure fronts for $i > 3$ cannot be seen on figure 4. Equations (9) and (10) are validated by our experimental results. As an example, using the test presented in figures 5 and 6, the experimental value of $C_{pi}, i \geqslant 2$ and the value predicted with equation (10) can be compared (see table 2). The value of α is then calculated using the values of C_{p0} and C_{p1}.

Once the transmission coefficient and amplitude of the incident compression wave are known, the amplitude of each small pressure step ($C_{p1}, C_{p2}, C_{p3}, \ldots$) may be estimated. Let us now focus on how the shape of a single pressure front gets distorted when passing through an opening. Figure 7 presents an (x, t) diagram describing the opening region; on this diagram, all pressure wavefronts are assumed to propagate at the speed of sound. The incident compression wavefront has been represented by the lines OC_{ih} and OC_{it}, being the head and tail of the incident wavefront, respectively. The length of the incident wavefront is denoted $L_{front\ i}$. The air discharge that occurs when passing through the opening yields a downstream compression wave, OC_t, of reduced amplitude (C_{pt}) and an equal front length ($L_{front\ t} = L_{front\ i}$).

The process by which the reflected pressure wave is generated proves different however. A difference in shape between the transmitted and reflected fronts could

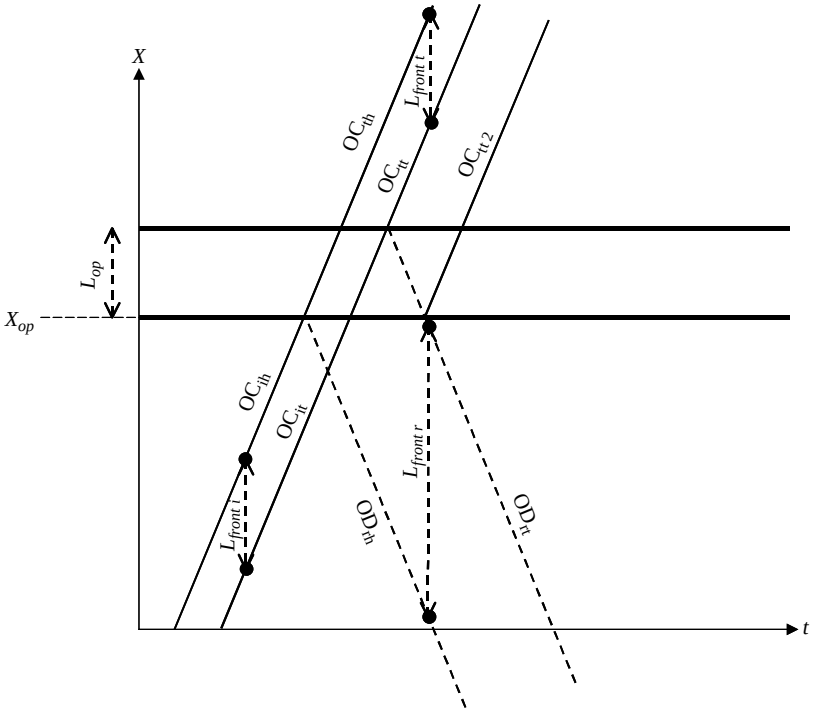

FIGURE 7. (x, t) diagram showing the tube opening.

nonetheless have been expected. Once the head of the incident front OC_{ih} reaches the opening, air discharge occurs, which then creates an expansion wave that propagates both downstream and upstream. This expansion wave lasts as long as the incident compression front is propagating into the open region of the tube, i.e. until wavefront OC_{it} reaches the downstream part of the opening. The spatial extent of the expansion front, called here the reflected front, is then

$$L_{front\ r} = L_{front\ i} + 2L_{op}. \tag{11}$$

Based on this one-dimensional representation of the phenomenon, the major parameters relevant to studying the effects of an opening on a compression wavefront can be identified. Both the α coefficient and shape of the successive transmitted and reflected pressure wavefronts are expected to be influenced by the following parameters, namely:

(i) the relative surface area of the opening with respect to the tube cross-section, S_{op}/S_{tube};

(ii) the amplitude of the incident compression wave, Δp_i; and

(iii) the relative length of the incident compression front with respect to the opening length, $L_{front\ i}/L_{op}$.

Section 6 of this paper is devoted to a close examination of the parameters. It should be noted that if the opening lies close to the tube entrance, the multiple reflections of compression and expansion waves between the opening and the tube entrance will interact. The resultant compression wavefront measured downstream from the opening will not be composed of separate fronts, as was the case in figure 6.

The next section will present the numerical computations performed to simulate the transmission–reflection process that is taking place within the opening.

4. Presentation of numerical computations

The aim of these numerical computations is to predict the amplitude and shape of both the transmitted and reflected pressure fronts. The one-dimensional propagation of pressure waves in the tube will be considered herein. Compression waves are generated in the computational domain by imposing an input mass flux at the inlet boundary. The shape of the incident compression wavefront can then be easily monitored. Pressure wavefronts from our experiments can also be imposed as a boundary condition. The entry of the slender body resulting in compression wave generation will not be considered here as this constitutes a separate and complex problem (Howe 1998; Ogawa & Fujii 1997). The multiple pressure wave reflections at both the tube entrance and opening are not simulated, and neither are the effects of wall friction and heat transfer. Air has been modelled as a perfect gas. Based on these assumptions, Euler equations in their conservative form are used in conjunction with a null source term along the tube, except in the opening region of the computation domain:

$$\frac{\partial U}{\partial t}+\frac{\partial f}{\partial x}=Q;\quad U=\begin{Bmatrix}\rho\\ \rho\cdot u\\ \rho\cdot e\end{Bmatrix};\quad f=\begin{Bmatrix}\rho\cdot u\\ p+\rho\cdot u^2\\ (\rho\cdot e+p)\cdot u\end{Bmatrix} \tag{12}$$

where e is the total energy per mass unit

$$e=\tfrac{1}{2}u^2+\frac{p}{(\gamma-1)\rho}.$$

$Q=0$ everywhere except at the opening location, where

$$Q=\begin{Bmatrix}-\dfrac{\phi_g}{S_{op}\Delta x}\\ 0\\ -\dfrac{\phi_g}{S_{op}\Delta x}h_g\end{Bmatrix}. \tag{13}$$

The index g relates to the fluid exiting the tube. Equation (13) is obtained by writing the mass conservation and total enthalpy conservation within a one-dimensional control volume with atmospheric surrounding conditions. The momentum equation remains unchanged since the outgoing/ingoing flow velocity is presumed to be oriented normal to the tube axis.

ϕ_g is the exiting mass flow rate, i.e. $\phi_g=C_D\cdot\rho_g v_g S_{op}$, with v_g deduced from the conservation of total enthalpy through the opening (the Saint-Venant relation):

$$v_g=\sqrt{\frac{2\gamma}{\gamma-1}\frac{p}{\rho}\left(1-\left(\frac{p_0}{p}\right)^{(1-1/\gamma)}\right)}. \tag{14}$$

C_D is the contraction coefficient of the opening. The geometry of the opening is constituted of one or more slits of the same type laid out around the perimeter of the tube (see § 2.3). The value of C_D is closely related to the specific geometry of the slit; this value is adjusted from experimental data: a single experimental measurement has been used to determine C_D and this unique value is then employed in all computations (see § 5). ρ_g is obtained by means of the following isentropic relation:

$$\frac{\rho_g}{\rho}=\left[1+\frac{\gamma-1}{2}\left(\frac{v_g}{c_0}\right)^2\right]^{-1/(\gamma-1)}. \tag{15}$$

The variable h_g represents the total enthalpy per mass unit:

$$h_g = \frac{\gamma}{\gamma - 1}\frac{p}{\rho}. \tag{16}$$

The second-order Mac-Cormack scheme will now be used. In order to attenuate oscillations, the predictor–corrector sequence is inverted at each time step, as proposed in Hoffmann & Chiang (1993). The CFL stability condition for this scheme is such that

$$\sigma = \max(|u| + c)\frac{\Delta x}{\Delta t} < 1. \tag{17}$$

In the absence of a source term, σ is commonly set equal to 0.95. In the presence of a source term however, stability is reached for $\sigma = 1/4$.

Inlet conditions are such that the velocity is subsonic, which imposes two separate variables: velocity u, and density ρ. The density is deduced from the imposed velocity value through application of the isentropic relation (15). Pressure at the inlet is then computed using compatibility relations based on resolutions of the characteristics curves (Hirsch 1990).

The extent of the computational domain is equal to the tube length used in the experiments. The spatial discretization is chosen in a way that the incident pressure front is represented by 200 points.

5. Validation of the numerical code

Pressure waves in the simulation propagate in a semi-infinite domain without friction effects. Numerical tests were performed in order to check the steepening of pressure wavefronts when propagating within the computational domain (i.e. no opening is present). When pressure wavefronts from those experiments with the highest amplitude (1600 Pa) are imposed at the inlet boundary of the computational domain, they propagate along a length of 40 tube diameters with no increase in pressure gradient.

In order to validate the numerical code, a compression wave measured under the conditions of Test case 4 has been imposed as an inflow condition. Figure 8 presents the computed and measured pressure signals at positions $X_{\mu phone\,1}$ and $X_{\mu phone\,2}$. Figure 9 shows the normalized pressure gradients of the incident, transmitted and reflected waves. The normalized pressure gradient is defined as $(\mathrm{d}p/\mathrm{d}t)/\Delta p_{max}$, where Δp_{max} is the maximum amplitude of the wavefront. This normalized pressure gradient proves to be convenient for comparing wavefronts with different amplitudes since in all cases,

$$\int_0^{t_{front}} \frac{(\mathrm{d}p/\mathrm{d}t)}{\Delta p_{max}}\mathrm{d}t = 1.$$

In the present case, $\Delta p_i = 1110$ Pa, $\Delta p_t = 620$ Pa and $\Delta p_r = -430$ Pa.

It should be pointed out that in contrast with equation (7), the sum of Δp_t and $|\Delta p_r|$ is not equal to Δp_i; this is due to the fact that the reflected wave measured at position $X_{\mu phone\,1}$ has been affected by a weak, yet noticeable, positive pressure wave originating from the tube entrance. This pressure wave, which follows the initial compression wave due to the body nose entry, results from friction effects along the moving body wall. This feature can be seen on figure 8 (dashed line). At position $X_{\mu phone\,1}$ therefore, competition between the expansion wave (the reflected wave) stemming from the opening and the compression wave stemming from the

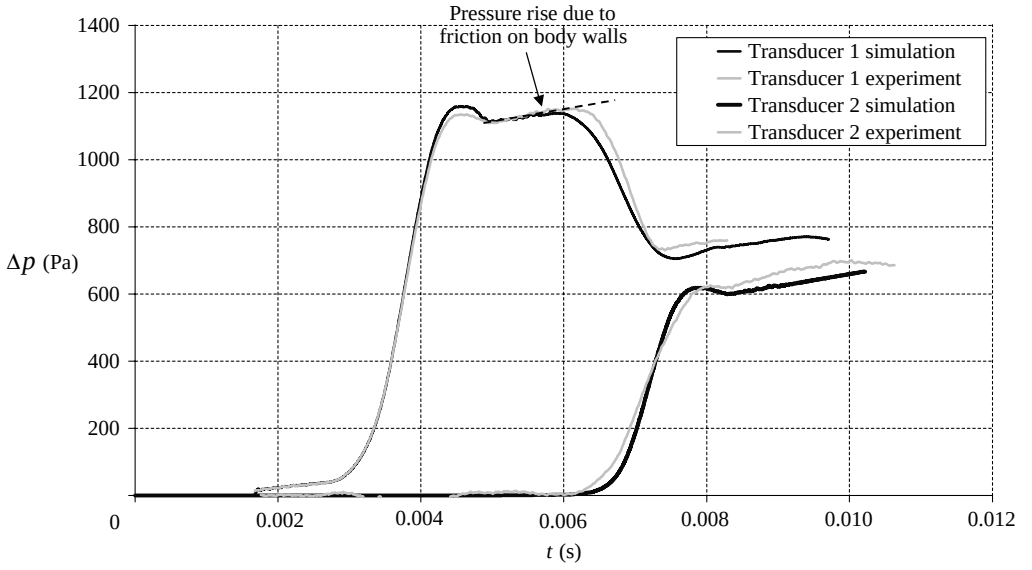

FIGURE 8. Measured and simulated compression wavefront at positions $X_{\mu phone\ 1}$ and $X_{\mu phone\ 2}$.

tube entrance is present. Simulations conducted with the primary compression wave alone (without the pressure rise due to friction effects on body walls) have confirmed equation (7).

The value of the contraction coefficient C_D is adjusted so that the amplitude of the numerical transmitted wavefront matches the experimental wavefront for Test case 4 and $\Delta p_i = 1200$ Pa: $C_D = 0.84 \pm 0.02$. This value is held constant for all simulations performed in this study.

The overall level of agreement between the experimental and numerical pressure fronts is quite good. Simulations and experiments predict that the shape of the reflected and transmitted fronts is identical to the incident front.

No attempt has yet been made to simulate friction effects occurring as the pressure wavefront propagates in the tube. This task is not trivial in that an unsteady friction coefficient has to be taken into account, thereby yielding a complicated model (Schultz & Sockel 1988; Vardy & Brown 2002). This deformation process is merely a second-order phenomenon for the problem considered and therefore does not alter the study's conclusions.

6. Parametric study

In this section, we will examine the individual influences of the parameters identified in § 3.

6.1. *Influence of the relative surface area of the opening on both α and the shape of the transmitted and reflected wavefronts*

For this section, the incident pressure wave amplitude, Δp_i, has been set at 1200 Pa and the relative length of the incident wavefront L_{front}/L_{op} lies within the range $L_{front}/L_{op} \gg 1$. This condition has been obtained in the experiments for a moving body speed of $43\,\mathrm{m\,s^{-1}}$. Test cases 1 to 8 are performed for this part of the work. Figure 10 presents both the experimental and numerical data of the trend in α vs. the

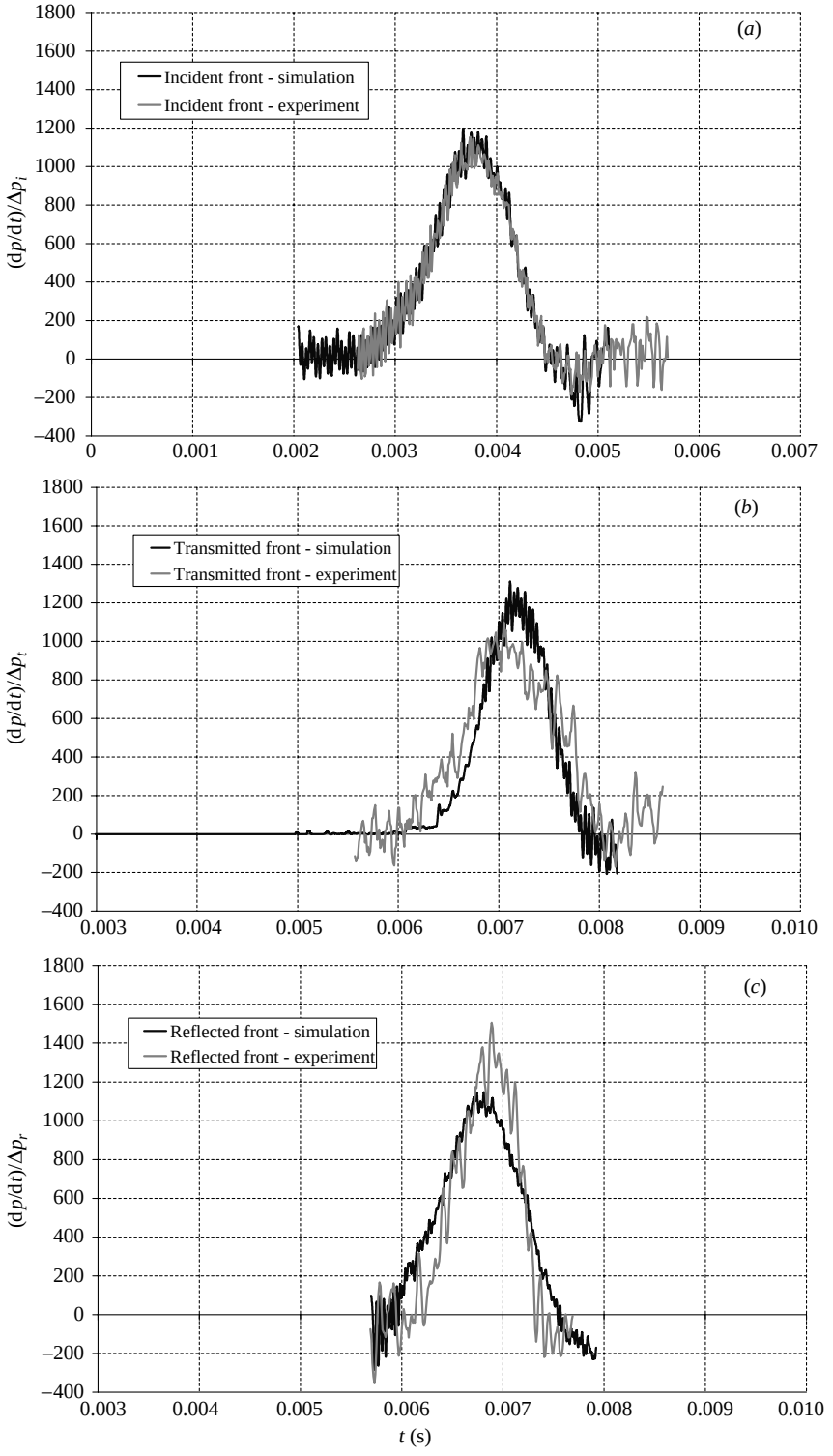

FIGURE 9. Normalized pressure gradient of the (*a*) incident, (*b*) transmitted and (*c*) reflected wavefronts.

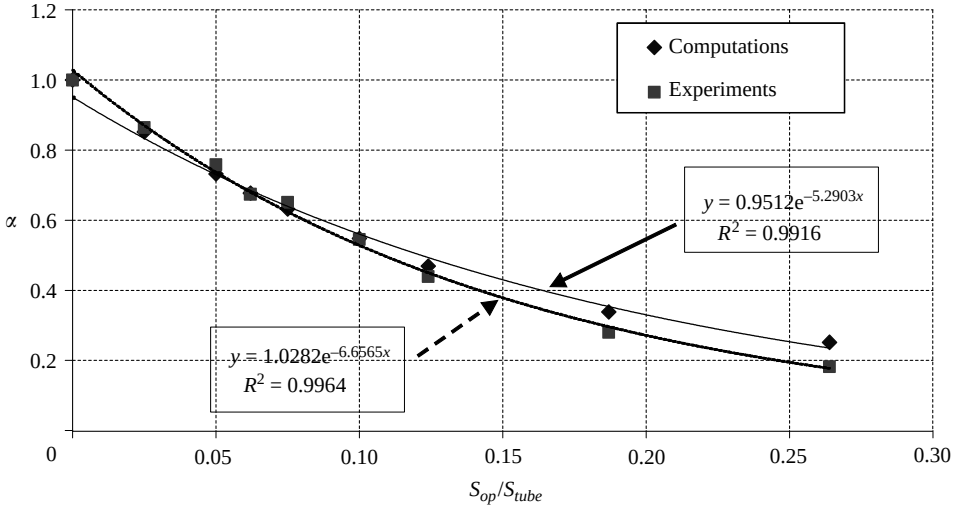

FIGURE 10. Evolution of transmission coefficient α with the relative surface area of the opening ($\Delta p_i = 1200$ Pa).

relative opening surface area with respect to the tube cross-section. The agreement between the two data sets is rather good. The experimental and numerical points are reported along with the best curve fit, which is an exponential function with a proportionality coefficient equal to -6.7 (experimental) and -5.3 (numerical), and a regression coefficient as high as 0.996 (experimental) and 0.992 (numerical). An exponential decrease in α with opening surface area is obtained both experimentally and numerically, with the decrease being slightly smaller in the computations. Note that a small opening surface area, $S_{op}/S_{tube} \approx 1/4$ (Test case 8), induces a rather low transmission coefficient, $\alpha \approx 0.2$.

For these simulations, the shape of the three wavefronts (incident, transmitted and reflected) has been closely examined using the representation of normalized pressure gradients. No influence of the relative surface area on the shape of the reflected and transmitted fronts has been observed.

6.2. *Influence of the incident compression wave amplitude on both α and the shape of the transmitted and reflected wavefronts*

For this section, the relative length of the incident wavefront L_{front}/L_{op} still lies within the range $L_{front}/L_{op} \gg 1$. The amplitude of the incident compression wave is varied from 400 Pa to 1600 Pa. Figure 11 presents the results obtained under these conditions for three different relative opening surface areas. For a given opening, the transmission coefficient increases with the incident compression wave amplitude; this evolution is logarithmic. Simulations are well-suited to predicting the influence of the incident compression wave amplitude on the transmission coefficient.

As far as the shape of the reflected and transmitted fronts is concerned, no influence of this amplitude has been observed.

6.3. *Influence of the relative incident wavefront length on both α and the shape of the transmitted and reflected wavefronts*

For this section, the relative surface area of the opening is set at 0.1 and the amplitude of the incident compression front at 1670 Pa. $L_{front\ i}/L_{op}$ is made to vary from 100 to 0.05. The results presented here have only been based on simulations, since the

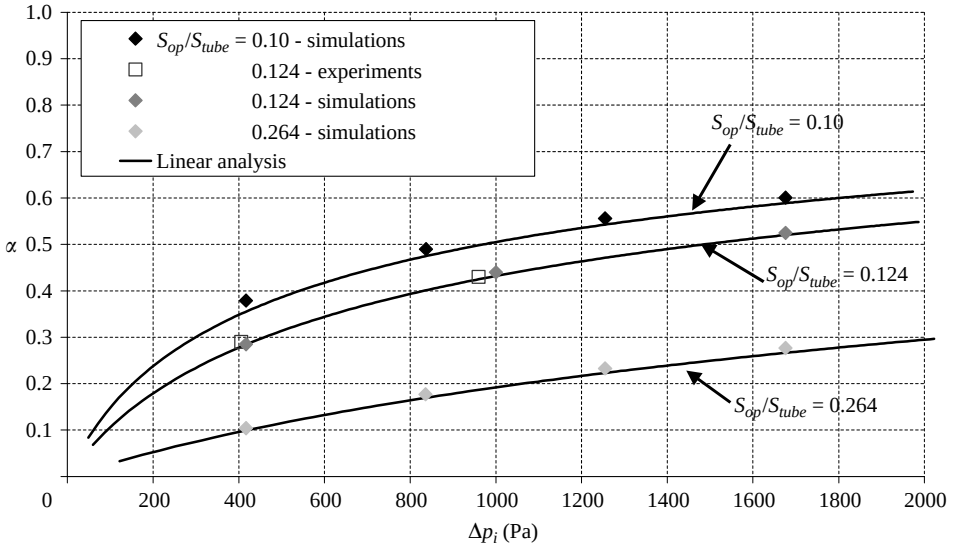

FIGURE 11. Evolution of transmission coefficient α with the amplitude of the incident compression wave for various relative surface areas of the opening.

experimental data are restricted to the case where $L_{front\,i}/L_{op} \gg 1$. The shape of the incident front has been chosen as linear, i.e. $\mathrm{d}p/\mathrm{d}t$ is constant. To derive results with $L_{front\,i}/L_{op} \ll 1$, it was decided to hold the length of the incident front fixed ($L_{front\,i} = 0.88\,\mathrm{m}$) and to increase the opening length. The computational domain is considerably extended in order to record the entire reflected pressure front at $X_{\mu\text{-}phone\,1}$. As an example, for $L_{front\,i}/L_{op} = 0.05$, $X_{\mu\text{-}phone\,1} = 20\,\mathrm{m}$, $L_{op} = 17.6\,\mathrm{m}$, $X_{\mu\text{-}phone\,2} = 40\,\mathrm{m}$, $L_{front\,r} = 36\,\mathrm{m}$ and $L_{tube} = 72\,\mathrm{m}$.

Figure 12 displays the influence of $L_{front\,i}/L_{op}$ on the transmitted front. For $L_{front\,i}/L_{op} \gg 1$, the amplitude and shape of the transmitted front remain constant. When $L_{front\,i}/L_{op}$ is of the order of 1, the amplitude of the transmitted front, and therefore α, decreases. This decrease lasts until $L_{front\,i}/L_{op} \ll 1$; this result is due to the existence of a compression wave that occurs when the reflected wave (wave OD_r on the sketch in figure 7) reaches the beginning of the opening (at position X_{op}). Part of this pressure wave reflects back as a compression wave at the end of the tube (wave OC_{t2} on the sketch in figure 7). This wave is only noticeable on the pressure signal at position $X_{\mu\text{-}phone\,2}$ when the length of the incident front reaches a value comparable to the opening length. For $L_{front\,i}/L_{op} \ll 1$, figure 12 shows that the transmitted front tends to steepen. As noted above, for $L_{front\,i}/L_{op} = 0.05$, the transmitted front is actually recorded at $X_{\mu\text{-}phone\,2} = 40\,\mathrm{m} = 900 D_{tube}$. Under these conditions, the weak numerical steepening of the compression wavefront due to nonlinear effects becomes significant.

Figure 13 presents the shape of the reflected fronts using the normalized pressure gradient depiction. The results obtained for $L_{front\,i}/L_{op}$ vary from 100 to 0.33. As mentioned in § 3, the length of the reflected front increases linearly with L_{op}. Equation (11) is confirmed by the series of simulations. For $L_{front\,i}/L_{op} < 1$, the reflected front becomes linear (as $\mathrm{d}p/\mathrm{d}t$ is constant) with the incident front. This section has shown that at the limit $L_{front\,i}/L_{op} \gg 1$, which corresponds to the actual opening encountered in railway tunnels, the shape of the transmitted front is identical to the incident front.

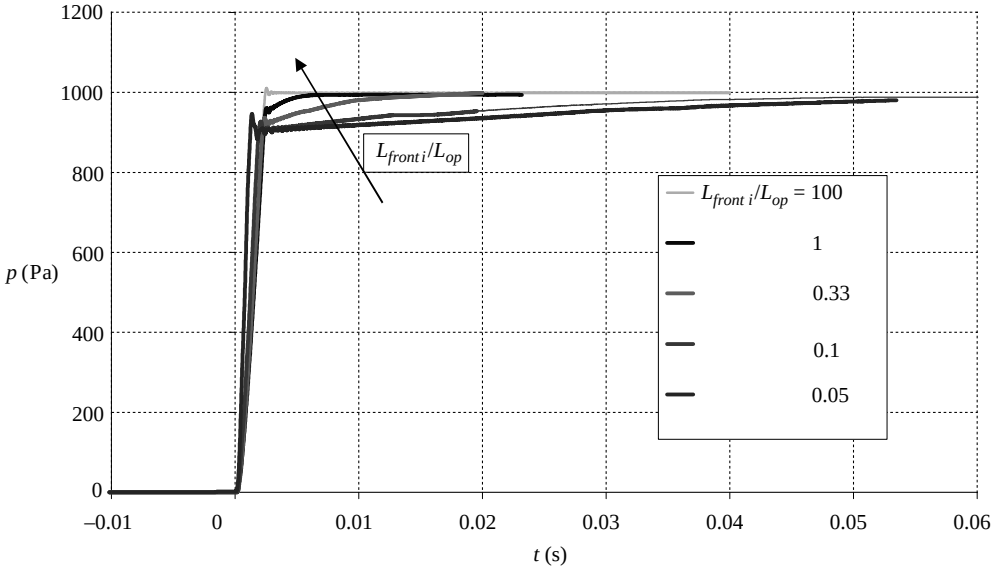

FIGURE 12. Evolution of the transmitted front with $L_{front\,i}/L_{op}$ ($\Delta p_i = 1670$ Pa and $S_{op}/S_{tube} = 0.1$).

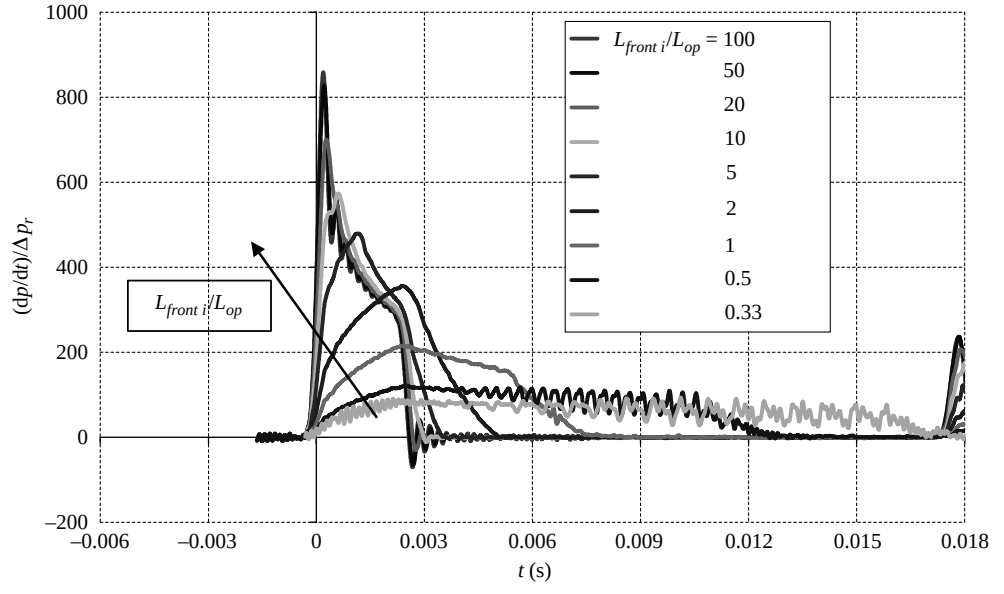

FIGURE 13. Evolution of the shape of the reflected front with $L_{front\,i}/L_{op}$ ($\Delta p_i = 1670$ Pa and $S_{op}/S_{tube} = 0.1$).

7. Linear analysis

Section 6 focuses primarily on the transmission process for a pressure wavefront propagating into a partially open portion of a tube. The results presented have been based on experiments and simulations conducted using Euler equations. This work provided us with greater understanding of the basic phenomena involved in problems of this type. The idea was then put forward that it was possible to predict

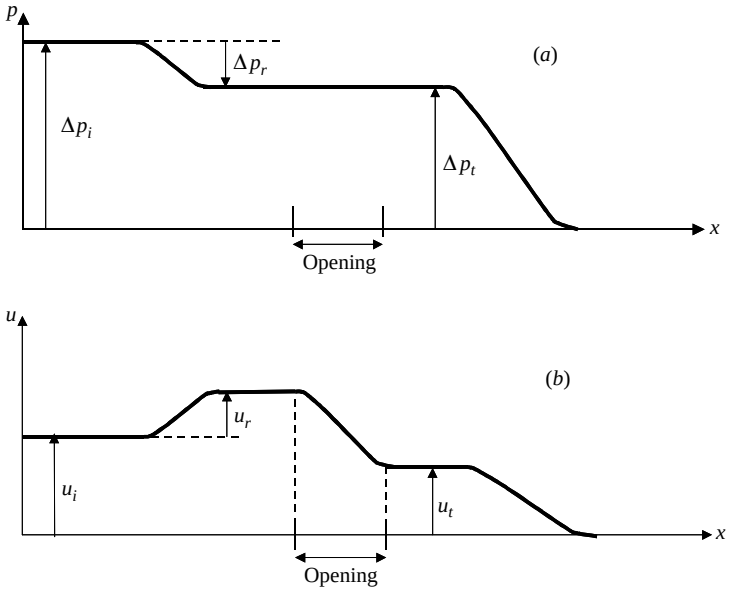

FIGURE 14. Sketch of the distribution of (*a*) pressure and (*b*) velocity along the tube in the region of the opening.

the transmission coefficient using both a linear acoustic approximation and the mass conservation equation. The transmission coefficient α depends mainly on two variables: the relative surface area of the opening S_{op}/S_{tube}, and the amplitude of the incident compression wave Δp_i. Let us now consider, for any value of the ratio $L_{front\,i}/L_{op}$, the time it takes for the incident pressure wavefront to completely pass the opening region, i.e. once the transmitted and reflected fronts have become fully developed. Figures 14(*a*) and 14(*b*) show a sketch of the spatial distribution of both pressure and velocity along the tube at that particular time. The control volume considered herein is the opening region. We can then write the mass conservation equation for this volume with one ingoing flow and two outgoing flows. The inflow (on the left side of figure 14) has a velocity of $u_i + u_r$. As seen on figure 14(*a*), the density in the opening is equal to the density behind the transmitted front ρ_t.

Using the notation introduced in § 4, the mass conservation equation is expressed as follows:

$$\rho_t(u_i + u_r)S_{tube} = C_D\rho_g v_g S_{op} + \rho_t u_t S_{tube}. \tag{18}$$

Since the ratio $\Delta p/p_0$ is of the order of 1–2 %, a first-order acoustic approximation may be developed. ρ is thus assumed to be constant. Using equation (7) and the linear acoustic approximation for determining the velocity behind a pressure front of amplitude Δp,

$$u = \frac{\Delta p}{\rho_0 c_0} \tag{19}$$

it then becomes possible to write

$$u_i = u_t + u_r. \tag{20}$$

Hence

$$u_i + u_r = 2u_i - u_t. \tag{21}$$

The Saint-Venant relation developed as a first-order expression leads to Bernoulli's equation:

$$v_g = \sqrt{\frac{2\Delta p_t}{\rho_0}} = \sqrt{2c_0 u_t}. \tag{22}$$

Equation (18) is then simplified to give

$$(2u_i - u_t)S_{tube} = C_D\sqrt{2c_0 u_t}S_{op} + u_t S_{tube}. \tag{23}$$

By noting that $\alpha = \Delta p_t/\Delta p_i = u_t/u_i$, equation (23) becomes

$$\alpha + C_D\sqrt{\frac{\rho_0}{2\Delta p_i}}\frac{S_{op}}{S_{tube}}c_0\sqrt{\alpha} - 1 = 0. \tag{24}$$

Equation (24) is a second-order equation; α, which is a positive solution to this equation, can thus be written as

$$\alpha = \frac{1}{4}\left[-C_D c_0\frac{S_{op}}{S_{tube}}\sqrt{\frac{\rho_0}{2\Delta p_i}} + \sqrt{C_D^2 c_0^2\left(\frac{S_{op}}{S_{tube}}\right)^2\frac{\rho_0}{2\Delta p_i} + 4}\right]^2. \tag{25}$$

This expression conveys an explicit dependence of α on both Δp_i and S_{op}/S_{tube}. Equation (25) allows one curve to be added to figure 10 (i.e. α versus S_{op}/S_{tube} for a fixed Δp_i) and another curve to figure 11 (i.e. α versus Δp_i for different S_{op}/S_{tube} values). The three approaches (experimental, numerical and analytical) used in this study are all found to be consistent with one another.

The present linear analysis has been compared with the analytical results obtained in Howe *et al.* (2003), as validated by reduced-scale measurements. Two cases are discussed in this paper. According to the first case, the train speed reaches $97.8\,\mathrm{m\,s^{-1}}$, the train/tunnel blockage ratio is 0.2 and the relative surface area of the opening is 0.102 (the opening is rectangular in shape with an aspect ratio of 2). Without any opening, the compression wave amplitude generated by train entry would be equal to $\Delta p_i = 3100\,\mathrm{Pa}$, as predicted with Ozawa's formulation. Equation (25) predicts $\alpha = 0.67$ with $C_D = 0.8$ and $\alpha = 0.71$ with $C_D = 0.7$. A value of around 0.7 can be read from figure 6. For the second case, the train speed is $96.7\,\mathrm{m\,s^{-1}}$, the train/tunnel blockage ratio 0.2 and the relative surface area of the opening 0.051; in this case, $\Delta p_i = 3000\,\mathrm{Pa}$ and equation (25) predicts $\alpha = 0.82$ with $C_D = 0.8$ and $\alpha = 0.84$ with $C_D = 0.7$. A value of around 0.85 can now be read from figure 7.

8. Conclusion

Introducing an opening along a tube with a limited cross-section ($S_{op}/S_{tube} < 1/4$) induces a considerable change in the compression wavefront produced by a slender body entry; it splits the original compression front into a series of smaller pressure steps. The process by which this front is formed results from successive pressure waves passing through the opening as well as their reflection between the tube entrance and the opening. Our analysis has proved that the amplitude of these successive pressure steps is governed by a mathematical series (equation (10)). The main parameter of this equation is what we have defined herein as the transmission coefficient α of the opening. The precise estimation of the resultant pressure front downstream of the

opening can then be reduced to the generic problem of a pressure wavefront passing through an opening.

A numerical and experimental study has focused on the transmission–reflection process that takes place when a pressure wavefront passes through an opening. Three major parameters have been identified for this problem: the relative opening surface area with respect to tube cross-section, the amplitude of the incident compression wave, and the relative spatial length of the compression wave with respect to the opening length.

For practical reasons, our experiments have been limited to the case where the length of the pressure front is large compared to the opening length. The numerical code then allows simulation of cases in which the length of the pressure front is considerably smaller than the opening length. The experiments have been satisfactorily reproduced by the computations. Both experiments and simulations show that the transmission coefficient through the opening decreases exponentially with the relative opening surface area and that as the incident front amplitude increases, the transmission coefficient becomes higher as well. The shape of the reflected and transmitted pressure fronts is similar to that of the incident front as long as the length of the incident front is large compared to the opening length. A linear analysis of the problem based on both the linear acoustic approximation and the continuity equation has demonstrated the ability to predict, in a simple manner, the transmission coefficient.

The hybrid numerical/experimental analysis developed in this paper results in a rather simple tool for predicting the effect of an opening on compression wave propagation. The transmission coefficient through the opening can indeed be estimated very accurately using the linear analysis developed in § 7. With equation (10), the amplitude of the successive pressure steps propagating downstream of the opening into the tunnel can now be accurately estimated (once the compression wave amplitude that would be formed without an opening, as predicted for example with Ozawa's formulation, is known). When a train enters a tunnel, the length of the compression wave is large in comparison not only with the tunnel diameter, but also with practical perforations that could be made along the tunnel. The present experiments and computations have thus indicated that the shape of the pressure fronts generated by the opening is identical in normalized representations. This prediction tool is consistent with the analytical formulation proposed by Howe *et al.* (2003) yet remains somewhat simpler to use.

The present paper leads to important conclusions for the design of openings in many countermeasures envisaged for the train/tunnel entry problem (perforated hood, use of side branches, etc.). First, it reveals that the opening surface area must be limited: a relative opening surface area of 0.25 leads to a transmission coefficient of about 0.25. Full-scale tests (Ozawa & Maeda 1988) have confirmed these conclusions. Secondly, when the body nose reaches the opening, it creates an additional pressure wave with an amplitude on the order of $(1-\alpha)C_{pi}$. This effect may prove to be sizable for a large opening surface. It therefore appears that the best opening surface area for the problem investigated would be one in which the transmission coefficient equals 0.5, i.e. $S_{op}/S_{tube} \approx 0.12$ for high-speed train tunnels.

Now that the physical phenomena involved in the transmission–reflection process, with a thin opening directly connected to the atmosphere, are believed to be well-understood, more complex configurations offering relevant applications for high-speed railway tunnel design may be undertaken; such configurations would include openings connected to side-branched pipes of varying lengths ending either in the open atmosphere or within an adjacent tunnel.

The authors are very grateful for the financial support provided by the French research program PREDIT 2 – AIVE (Aérodynamique Instationnaire des Véhicules terrestres et de leur Environnement). Special thanks are also addressed to Mr Xavier Riviere for his very precise experiments and to Professor Tadashi Kageyama for his constant support and most valuable advice.

REFERENCES

Auvity, B. 1998 Phénomènes aérodynamiques instationnaires générés par l'entrée d'un train dans un tunnel. PhD Dissertation of the University of Poitiers.

Auvity, B., Bellenoue, M. & Kageyama, T. 2001 Experimental study of the unsteady aerodynamic field outside a tunnel during a train entry. *Exps. Fluids* **30**, 221–228.

Bellenoue, M., Auvity, B. & Kageyama, T. 2001 Blind hood effects on the compression wave generated by a train entering a tunnel. *Expl. Therm. Fluid Sci.* **25**, 397–407.

Bellenoue, M. & Kageyama, T. 2002 Train/tunnel geometry effects on the compression wave generated by a high-speed train, TRANSAERO – A European Initiative on Transient Aerodynamics for Railway System Optimisation. *Brite/Euram Project "Transient Aerodynamics for Railway System Optimisation"* (ed. B. Schulte-Werning, R. Gregoire, A. Malfatti & G. Matschke), pp. 276–289. Springer.

Bellenoue, M., Moriniere, V. & Kageyama, T. 2002 Experimental 3D-simulation of the compression wave due to train-tunnel entry. *J. Fluids Struct.* **16**, 581–595.

Henson, D. A. & Pope, C. W. 1997 The alleviation of pressure transients in a main line railway tunnel. 9th *Intl. Symp. on Aerodynamics and Ventilation of Vehicles Tunnels, Aosta, Italy.*

Hirsch, C. 1990 *Numerical Computation of Internal and External Flows*, vol. 2. John Wiley and Sons.

Hoffmann, K. A. & Chiang, S. T. 1993 *Computational Fluid Dynamics for Engineers*, vol. 2. Engineering Education System.

Howe, M. S. 1998 The compression wave produced by high speed train entering a tunnel. *Proc. R. Soc. Lond.* A **454**, 1523–1534.

Howe, M. S. 1999 On the compression wave generated when a high-speed train enters a tunnel with a flared portal. *J. Fluids Struct.* **13**, 481–498.

Howe, M. S., Iida, M., Fukuda, T. & Maeda, T. 2003 Aeroacoustics of a tunnel-entrance hood with a rectangular window. *J. Fluid Mech.* **487**, 211–243.

Iida, M., Matsumura, T., Nakatani, K. Fukuda, T. & Maeda, T. 1996 Optimum nose shape for reducing tunnel sonic boom. *Institution of Mechanical Engineers Paper* C514/015/96.

Maeda, T., Matsumura, T., Iida, M., Nakatani, K & Uchida, K. 1993 Effect of shape of train nose on compression wave generated by train entering tunnel. *Intl. Confe. on Speedup Technology for Railway and Maglev Vehicles* Nov. 22–26 1993, pp. 315–319.

Ogawa, T. & Fujii, K. 1997 Numerical investigation of three-dimensional compressible flows induced by a train moving into a tunnel. *Computers Fluids* **26**, 565–585.

Ozawa, S. 1979 Study of micro-pressure wave radiated from a tunnel exit. *Railway Technical Research Report* (in Japanese).

Ozawa, S. & Maeda, T. 1988 Tunnel entrance hoods for reduction of micro-pressure wave. *Q. Rep. RTRI* **29**(3), 134–139.

Schultz, M. & Sockel, H. 1988 The influence of unsteady friction on the propagation of pressure waves in tunnels. 6th *Intl Symp. on Aerodynamics and Ventilation of Vehicles Tunnels, Durham, England.*

Vardy, A. & Brown, J. 2002. An overview of wave propagation in tunnels, TRANSAERO – A European Initiative on Transient Aerodynamics for Railway System Optimisation. *Brite/Euram Project "Transient Aerodynamics for Railway System Optimisation"* (ed. B. Schulte-Werning, R. Grégoire, A. Malfatti & G. Matschke), pp. 249–266. Springer.